Energy, Environmental, and Catalysis Applications

Hydrogen-Bonding Interactions in Hybrid Aqueous/Non-Aqueous Electrolyte Enables Low-Cost and Long-Lifespan Sodium-Ion Storage

Rodney Chua, Yi Cai, Pei Qi Lim, Sonal Kumar, Rohit Satish, William Jr Manalastas, Hao Ren, Vivek Verma, Shize Meng, Samuel Morris, Pinit Kidkhunthod, Jianming Bai, and Madhavi Srinivasan

ACS Appl. Mater. Interfaces, **Just Accepted Manuscript** • DOI: 10.1021/acsami.0c03423 • Publication Date (Web): 28 Apr 2020

Hydrogen-Bonding Interactions in Hybrid Aqueous/Non-Aqueous Electrolyte Enables Low-Cost and Long-Lifespan Sodium-Ion Storage

Rodney Chua, [a] *Yi Cai,* [a] *Pei Qi Lim,* [a] *Sonal Kumar,* [a] *Rohit Satish,* [b] *William Manalastas Jr.,* [a] *Hao Ren,* [a] *Vivek Verma,* [a] *Shize Meng,* [a] *Samuel A. Morris,* [a] *Pinit Kidkhunthod,* [c] *Jianming Bai,* [d] *and Madhavi Srinivasan* [a, *]

[a] School of Materials Science and Engineering, Nanyang Technological University, 11 Faculty Ave, Singapore 639977, Singapore

E-mail: madhavi@ntu.edu.sg

[b] Energy Storage and Distributed Resources Division, Lawrence Berkeley National Laboratory, 1 Cyclotron Road, Berkeley, 94720, USA

[c] Synchrotron Light Research Institute (Public Organization), Muang, Nakhon Ratchasima, 30000, Thailand

[d] Synchrotron Light Source II, Brookhaven National Laboratory, Upton, NY 11973, USA

Abstract

Although "water-in-salt" electrolytes have opened a new pathway to expand the electrochemical stability window of aqueous electrolytes, the electrode instability and irreversible proton co-insertion caused by aqueous media still hinder the practical application, even when using exotic fluorinated salts. In this study, an accessible hybrid electrolyte class based on common sodium salts is proposed, and crucially an ethanol-rich media is introduced to achieve highly stable Na-ion electrochemistry. Here, ethanol exerts a strong hydrogen-bonding effect on water, simultaneously expanding the electrochemical stability window of the hybridized electrolyte to 2.5 V, restricting degradation activities, reducing transition metal dissolution from the cathode material and improving electrolyte-electrode wettability. The binary ethanol-water solvent enables the impressive cycling of sodium-ion batteries based on perchlorate, chloride, and acetate electrolyte salts. Notably, a $Na_{0.44}MnO_2$ electrode exhibits both high capacity (81 mAh g^{-1}) and remarkable long cycle life >1000 cycles at 100 mA g^{-1} (a capacity decay rate per cycle of 0.024%) in a 1 M sodium acetate system. The $Na_{0.44}MnO_2$/Zn full cells also show excellent cycling stability and rate capability in a wide temperature range. The gained understanding of the hydrogen-bonding interactions in the hybridized electrolyte can provide new battery chemistry guidelines in designing promising candidates for developing low cost and long lifespan batteries based on other (Li^+, K^+, Zn^{2+}, Mg^{2+}, and Al^{3+}) systems.

Keywords: hybrid, hydrogen-bonding, rechargeable sodium-ion batteries, $Na_{0.44}MnO_2$, electrolyte

Introduction

Towards a green and sustainable large-scale scale stationary energy storage systems (ESSs), aqueous rechargeable sodium-ion batteries (ARSIBs) is considered as one of the promising candidates due to safer battery electrolytes and the abundance of low-cost sodium resources.[1-4] However, ARSIBs are prone to suffer from inferior cycling stability, owing to the parasitic side reactions associated with the aqueous electrolyte system, such as limited operating voltage window (~1.23V) induced by the H_2/O_2 evolution reactions, dissolution of electrode materials and water protons co-insertion into the host electrode, all of which have hampered their practical applications.[1-2, 4]

Recently, a new class of electrolytes, namely "water-in-salt" electrolytes, constituted from high-concentration salts, have been explored.[5-8] For instance, an electrolyte such as $NaCF_3SO_3$ (9.26 mol kg^{-1}, 9.26 m), can expand the operational voltage window from 1.23 to 2.50 V and suppress hydrogen evolution through the formation of solid-electrolyte interphase (SEI) on the anode, thereby granting access to high-energy Na-ion batteries. An aqueous Na-ion full battery by using $Na_{0.66}[Mn_{0.66}Ti_{0.34}]O_2$ as the cathode, $NaTi_2(PO_4)_3$ as the anode and 9.26 m $NaCF_3SO_3$ as the electrolyte, can achieve a superior long-term cycle life of >1200 cycles at 1C.[5] However, the cell still suffered an obvious capacity fading in the initial few cycles with a low capacity of ~20 mAh g^{-1} after 100 cycles. Even in 9.2 m saturated $NaCF_3SO_3$ electrolyte, the molar ratio of water to sodium-ions (6.5) remains high, because of the relatively low solubility of sodium salts with fluorinated anions. Hence, there is still a relatively large amount of free water in the electrolyte, which may lead to electrode instability. In addition, the high cost of these "water-in-salt" electrolytes (Table S1) has inevitably hindered their practical applications.

It is well known that each water molecule consists of one heavier oxygen atom and two lighter hydrogen atoms. In liquid water, the hydrogen atoms in a molecule are attracted to the oxygen atoms from neighboring water molecules and form hydrogen bonds. The hydrogen

bonds between water molecules are constantly breaking and reforming on picosecond time scales.[9] Since hydrogen-bonding plays an essential role in the physical, chemical, and structural properties of liquid water, selectively and significantly strengthen the hydrogen-bonding strength of water by introducing a polar protic solvent could be an alternative low-cost approach to suppress water activity. Ethanol (dielectric constant ε = 25.10, dipole moment 1.70) as a polar protic solvent, is fully miscible with water (dielectric constant ε = 80.10, dipole moment 1.84).[10-11] By hybridizing ethanol with water solvents, there will be a structure rearrangement through the breaking of the water hydrogen-bonding network and forming a new type of hydrogen bond organization.[12-14] This would decrease the interfacial tension of ethanol-water cosolvent, which is favorable for better electrode/electrolyte contact. In addition, the low freezing point (-114 °C) of ethanol could potentially expand the hybrid electrolyte working temperature range.[15]

Herein, we report a new type of hybrid electrolyte prepared by using binary ethanol-water solvents. Such solvents are readily available, cost-effective, and can accommodate various low-concentration sodium salts, such as chlorides, perchlorates, and acetates, enabling Na-ion chemistries with high performance especially excellent cycling stability. In the ethanol-water system, ethanol plays an active role in rearranging the network structures of water molecules *via* hydrogen-bonding, thereby enabling intimate electrode-electrolyte contact and suppressing the protons co-insertion into the electrode upon cycling and reducing the dissolution of Mn from the cathode. An electrolyte consisting of 1 M sodium acetate in 5:1 *v/v* ethanol-water (denoted as 1 M NaAc-Et/Di) system exhibits strong hydrogen-bonding interactions and excellent wettability, which allows a $Na_{0.44}MnO_2$ electrode to deliver a high discharge capacity of 81 mAh g^{-1} at 100 mA g^{-1} with remarkable reversibility. Superior long-term cycle life of >1000 cycles (a capacity decay rate per cycle of 0.024%) was also achieved. Furthermore, *ex-situ* XRD, SEM, and TEM-EDX studies of the $Na_{0.44}MnO_2$ electrodes demonstrate that a

considerable number of protons can co-insert into the lattice of $Na_{0.44}MnO_2$ in 1 M NaAc-Di system, finally leading to irreversible phase collapse (MnOOH). In comparison, the crystal structure of $Na_{0.44}MnO_2$ is maintained in the Et/Di system, indicating that hydrogen-bonding with the water molecules would be an effective way to improve the cycling stability. This approach guides a new direction for the development of sodium-ion battery with excellent cycle life for green and sustainable large-scale practical applications.

Results and discussion

Cosolvents of ethanol-water are prepared by mixing the two components in different volume ratios. For convenience, the various ethanol-water volume ratios used will be denoted as x: y Et-Di. To investigate the influence of solvent composition on the surface wettability, contact angles of various ethanol-water solvents were measured and presented in Figure 1a. It can be found that the presence of ethanol in the solvent system results in a ubiquitous reduction in the contact angle when compared to that of Di water (85.9°). The decrease in contact angle becomes increasingly pronounced with larger ethanol content. Due to four-coordinations involving two donor and two acceptor hydrogen bonds, water exhibits a three-dimensional tetrahedral hydrogen-bonding network. Because of the relatively high attraction among water molecules through the hydrogen-bonding network, water has high surface tension.[16] By the introduction of ethanol, new ethanol-water interactions (cross association) occur. The addition of ethanol in water breaks the water hydrogen-bonding network, resulting in a decrease of the water-water hydrogen bonds. As a result, the interfacial tension of ethanol-water cosolvent is decreased, which is consistent with the previous report.[17] Overall, the ethanol-water system shows a significant improvement in terms of wettability as compared to the Di water system. From the results, the 5:1 Et-Di system displays the lowest contact angle (19.2°) among all samples. It is predicted that using the 5:1 Et-Di system as electrolyte would allow a better

electrode penetration, critical to enhanced electrochemical performances.[18] This will be verified in later experiments in this paper.

In ethanol-water solvents, ethanol readily forms hydrogen bonds with water molecules.[19] To verify the existence and evaluate the strength of hydrogen bonds in ethanol-water solvents, a combination of spectroscopy techniques such as confocal Raman, Fourier-transformed infrared-attenuated total reflectance (FTIR-ATR) and ^{1}H nuclear magnetic resonance (NMR) were employed. Figure 1b shows the Raman scattering spectra of Di water and the various ethanol-water solvents at different volume ratios from 2700 cm^{-1} to 4000 cm^{-1}, which is the wavenumber range focusing on the vibrational modes of interest (CH_2, CH_3 and O-H bonds), whereas the supplementary lower wavenumber regions are presented in Figure S1. A full assignment for each peak is detailed in Table S2. As shown in Figure 1b, Di water exhibits symmetric O-H stretching (~3254 cm^{-1}) and asymmetric O-H stretching vibration (~3411 cm^{-1}) modes that form a broad Raman band owing to the abundant hydrogen-bonding environments among the water molecules.[13, 19-21] Additionally, a weak shoulder peak located around ~3613 cm^{-1} corresponds to the free O-H of water molecules.[19] Upon introduction of ethanol to the Di water, the peaks attributed to the symmetric (~2878cm^{-1}) and asymmetric (~2971 cm^{-1}) stretching modes of CH_3 as well as the CH_2 stretching mode (~2926cm^{-1}) of ethanol start to appear in the ethanol-water spectra.[13] As the volume ratio of ethanol to water increases, the O-H stretching bands display a distinct reduction in amplitudes, and the shoulder peak (~3613 cm^{-1}; free O-H) weakens until its complete disappearance. These results indicate that the hydrogen-bonding interactions among water molecules have been significantly weakened by increasing ethanol content. Meanwhile, the free O-H species activity has been largely suppressed. Moreover, the stretching modes of CH_2 and CH_3 exhibit redshift towards the lower wavenumber (Figure S2), indicating the new formation of hydrogen bonds between ethanol and water associates.[13, 19, 22-23]

The effect of hydrogen bonds between ethanol and water molecules was further explored using FTIR spectroscopy, as displayed in Figures 1c and S3. Since the O-H stretching bands in IR spectra for Di water overlap with that of ethanol (Figure S3), the water (H-O-H) bending vibrational band was used instead for evaluating the strength of hydrogen bonds in the various ethanol-water systems (Figure 1c).[12, 24] As the ethanol concentration increases, the H-O-H bending vibrational bands exhibit blueshift behavior towards the higher wavenumber region, indicating that the hydrogen bonds of water hydrogens become stronger.[12] This is possibly due to the strengthened hydrogen-bonding interactions between water hydrogens and ethanol oxygens with increasing ethanol content.

To further understand the interplay of hydrogen bonds between ethanol and water and confirm the ratios of the different types of protons associated with the CH_2, CH_3, and O-H groups in the binary co-solvents, we performed ^1H nuclear magnetic resonance (NMR) measurements. Figures 1d and S4 present the ^1H chemical shifts for the Di water, ethanol, and binary ethanol-water samples. As shown in Figure 1d, the protons associated with the O-H group for Di water and ethanol exhibit chemical shift values of 4.77 and 5.86 ppm, respectively. The O-H peaks for the ethanol-water mixtures show intermediate values of chemical shift, exhibiting a gradual downfield shift behavior towards higher ppm with increasing ethanol content. This indicates that the hydrogen atoms on the hydroxyl groups are increasingly deshielded as the ethanol concentration is increased, which suggests a corresponding increase in strength of the hydrogen bonds formed in ethanol-water solvents. Among all the binary solvents investigated, it should be highlighted that the 5:1 Et-Di system depicts the highest downfield shift (5.28 ppm). It also exhibits the lowest proton ratio number associated with the O-H group (calculated and presented in Figure 1e and Table S3 using the proton ratios of hydroxyl with water, CH_2, and CH_3).[25] This demonstrates the strong hydrogen-bonding

interaction between the ethanol and water molecules in the 5:1 Et-Di system. As such, the 5:1 Et-Di system would be subject to further studies in this paper.

Based on the above results, as discussed, the simplified structure models representing the water-water molecular interactions and ethanol-water (5:1 Et-Di) molecular association are illustrated in Figure 1f and g, respectively. In the Di water system (Figure 1f), the water molecules are weakly hydrogen bonded with the presence of free water molecules. On the other hand, in the binary ethanol-water system (Figure 1g), due to the existence of ethanol, the water-water bonds are broken, resulting in a reorganized network structure of water molecules through hydrogen-bonding with the hydroxyl group of ethanol. Meanwhile, the protons of free water molecules are also hydrogen bonded with ethanol oxygens. Therefore, it is highly anticipated that the 5:1 Et-Di system could suppress water protons activity and represent an ideal solvent for electrolytes to be used in ARSIBs, potentially enabling electrode stability and long-lasting cell cycle life.

Manganese-based oxides have been widely employed as active materials for energy storage due to its high capacity and rate performance.[26-36] In particular, $Na_{0.44}MnO_2$ (NMO) with a stable tunnel structure is attractive due to its unique large tunnels suitable for sodium insertion/extraction.[33, 37-40] Therefore, NMO has been chosen as the model cathode material to evaluate the efficacy of the Et/Di system in enhancing the cell cycling stability for this study.The NMO was prepared *via* an optimized polyvinylpyrrolidone (PVP)-assisted sol-gel synthesis method.[35] The crystal structure of the as-synthesized NMO was characterized by X-ray powder diffraction (XRD). As shown in Figure 2a, the diffraction peaks of the NMO sample can be well-indexed to the orthorhombic $Na_{0.44}MnO_2$ phase (PDF: 04-018-3147) with *Pbam* space group, which is in good agreement with a previous report.[34] Based on the Rietveld structure refinement, the lattice parameters of NMO are found to be a = 9.0897(6) Å, b = 26.427(2) Å, c = 2.8250(2) Å, with a lattice volume of 678.60(8) $Å^3$. The structure parameter

is summarized in Table S4. The crystal structure of $Na_{0.44}MnO_2$ is shown in the inset of Figure 2a. Three sodium sites can be found within the NMO tunnel-shaped framework formed by the corner-sharing (MnO_5) and edge-sharing (MnO_6) polyhedrons. One sodium site (Na 1) is located in the O-shaped tunnels, whereas two sodium sites (Na 2 and Na 3) are situated in the larger S-shaped tunnels.[26, 29, 33, 38, 41-43] Scanning electron microscopy (SEM) imaging (Figure 2b) further shows the uniformly yielded NMO plates with lengths of 3.0–5.0 μm and widths of 1.5–4.0 μm. In addition, the high-resolution transmission electron microscopy (HRTEM) image of NMO plates (Figure 2c) exhibits lattice fringe spacings of 0.45 nm, corresponding to the (200) plane of $Na_{0.44}MnO_2$, consistent with the XRD analyses.

To verify the hypothesis of modifying hydrogen-bonding interactions in ethanol-water enabling the suppression of water protons activity, 5:1 Et-Di, and De-ionized water systems were used as electrolytes to test three-electrodes cells with NMO, platinum foil and saturated silver/silver chloride (Ag/AgCl) as positive, counter and reference electrodes, respectively. 1 M sodium acetate (NaAc) was fully dissolved in varied ethanol-water mixtures to yield homogeneous electrolytes. Cycling voltammetry (CV) measurement was applied to evaluate the electrochemical window of 1 M NaAc-Di and -Et/Di electrolytes by using Ti mesh and Pt counter electrodes in three electrodes configuration. As shown in Figure 3a, the 1 M NaAc-Et/Di provides a wider electrochemical window than that of 1 M NaAc-Di electrolyte. The overall electrochemical stability window of 1 M NaAc-Et/Di electrolyte is ~2.5 V, which is larger than that of 1 M NaAc-Di electrolyte (~1.8 V). Ionic conductivity of 1 M NaAc-Et/Di electrolyte was further measured. The 1 M NaAc-Et/Di electrolyte shows an ionic conductivity of 6.01 mS cm^{-1}. It is 2-11 times higher than those of previously reported ionic liquid-based electrolytes for Na batteries, such as 1 M $NaClO_4$ in butylmethylpyrrolidinium-bis(trifluoromethanesulfonyl)imide (BMP-TFSI) ionic liquid electrolyte (1.00 mS cm^{-1}), and comparable to those of previously reported conventional organic electrolytes for Na batteries

(e.g., 1 M $NaClO_4$ in ethylene carbonate/dimethyl carbonate (EC: DMC, 30:70 wt%) has an ionic conductivity of ~5.00 mS cm^{-1}).[44-48] Then, based on the salt solubility, two more sodium-based salts sodium chloride (0.1 M NaCl), sodium perchlorate (1 M $NaClO_4$) were also fully dissolved to yield a series of electrolytes. The electrochemical performances of NMOs cycled in the various electrolytes were evaluated by galvanostatic charge-discharge (GCD) measurements (Figure S5), and their capacity retentions were recorded in Table S5. As expected, NMOs have shown superior cycling stability in Et/Di system as compared to that of the Di water system, regardless of the identity of the dissolved salt component. Specifically, the NMO cycled in 1 M NaAc-Et/Di electrolyte exhibited the best cycling performance with high capacity retention up to 99.0 % after 100 cycles.

Inspired by this observation, a series of electrochemical measurements were further conducted on NMO cycled in 1 M NaAc-Di and -Et/Di electrolytes to gain insight into the electrode kinetics. Cyclic voltammetry (CV) measurement was first performed at a scan rate of 0.1 mV s^{-1} between -0.4 V to 0.7 V *vs.* Ag/AgCl. Figures S6 and 3b depict the CV curves of NMO cycled in 1 M NaAc-Di and -Et/Di electrolytes, respectively. Seven pairs of redox peaks were found in both systems, corresponding to the de/insertion processes of sodium-ions at the various sites (Na 1, Na 2, and Na 3), as summarized in Table S6.[38, 42] Notably, in the first cathodic scan, the redox peaks of NMO cycled in 1 M NaAc-Di are weaker and broader (Figure S6), as compared to that of NMO cycled in 1 M NaAc-Et/Di (Figure 3b). This is mainly due to the partial sodium-ions (Na^+) leakage through the substitution of protons (H^+) in the Di water system.[49] From the second cycle onward, the CV profiles of NMO cycled in 1 M NaAc-Di show a significant reduction of current intensity, especially for redox peak III and peaks (V-VII) that correspond to the Na 3 and Na 2 sites, respectively.[38, 42] In general, sodium-ions located at Na 2 and Na 3 sites sharing the S-shaped tunnel would experience higher electrostatic repulsion than that of the sodium-ions located at Na 1 site in the O-shaped tunnel.[42] Therefore,

due to the proton-rich environment, it is postulated that the Di system could have favored the co-intercalation of protons into the NMO structure, inducing a higher electrostatic repulsion in S-shaped tunnel, hindering further sodium-ions insertion process, resulting in the poor cycling stability. In stark contrast, the NMO cycled in 1 M NaAc-Et/Di exhibits overlapping CV curves, indicating its highly reversible sodium de/insertion process (Figure 3b). This can be attributed to the suppressed water protons co-insertion. Due to the hydrogen-bond interaction of ethanol and water, the water activity has been successfully suppressed.

Figures 3c and d compare the galvanostatic discharge-charge profiles of NMOs tested in both 1 M NaAc-Di and 1 M NaAc-Et/Di, respectively. As shown in Figure 3c, the NMO cycled in 1 M NaAc-Di can deliver an initial discharge capacity of 71.6 mAh g^{-1} at 100 mA g^{-1}. Subsequently, it can only maintain a capacity of 55.4 mAh g^{-1} after five cycles, with an irreversible capacity loss of 22.6 %. In contrast, the discharge capacity of NMO cycled in 1 M NaAc-Et/Di is higher than of those cycled in 1 M NaAc-Di (Figure 3d). More strikingly, the NMO cycled in 1 M NaAc-Et/Di can maintain a capacity of 76.8 mAh g^{-1} after five cycles without any capacity loss, which is in good agreement with the excellent reversibility indicated from the overlapping curves as shown in previous CV results. Moreover, similar phenomena can be found for NMOs tested in 0.1 M NaCl and 1 M $NaClO_4$ in both electrolyte systems (Figures S7 and S8), demonstrating the excellent sodium diffusion kinetics of NMO cycled in Et/Di system. This may be ascribed to the intrinsic hydrogen-bonding interaction between the water protons and ethanol oxygen in the Et/Di system, which can effectively suppress the water protons activity.

To understand the variation of manganese oxidation state, we performed synchrotron X-ray absorption near edge structures (XANES) measurement. Figure 3e shows the normalized Mn K-edge profiles of the first fully discharged NMO electrodes as well as the pristine NMO electrode and commercial reference powders. The Mn K-edge of the NMO pristine electrode

resembles the characteristic absorption edge close to the MnO_2 (Mn^{4+}) reference powder, which indicates an average manganese valence state close to +4. On discharge, the Mn K-edge of the NMOs shift towards the lower energy as core-level binding energy changes with respect to the atomic valence states, indicating a reduction in the manganese valence state.[50] Interestingly, NMOs cycled in the two different electrolytes exhibit an apparent difference in the Mn oxidation state. The Mn K-edge of the fully discharged NMO in 1 M NaAc-Et/Di almost resembles the characteristic Mn K-edge of the Mn_2O_3 (Mn^{3+}) reference powder, indicating an average manganese valence state close to +3. On the other hand, the Mn K-edge of the fully discharged NMO in 1 M NaAc-Di exhibits an absorption edge between the characteristic Mn K-edges of MnO (Mn^{2+}) and Mn_2O_3 (Mn^{3+}) reference powders, indicating the mixed of +2 and +3 valence states. The presence of the Mn^{2+} species is indicative of the disproportionation reaction of the trivalent Mn species ($Mn^{3+}_s \rightarrow Mn^{4+}_s + Mn^{2+}_{aq}$),[30-31, 51] which could lead to Mn dissolution, resulting in the loss of active material.[42] Therefore, this could be the possible reason for the drastic capacity fading observed in the NMO when cycled in 1 M NaAc-Di electrolyte as opposed to a high capacity retention of NMO cycled in 1 M NaAc-Et/Di.

The rate capabilities of NMOs cycled in 1 M NaAc-Di and -Et/Di were further studied at various current densities, as shown in Figure 3f. Notably, NMO cycled in 1 M NaAc-Et/Di exhibits much better rate capability: 90.8 mAh g^{-1} (50 mA g^{-1}), 81.0 mAh g^{-1} (100 mA g^{-1}), 67.6 mAh g^{-1} (200 mA g^{-1}) and 42.2 mAh g^{-1} (500 mA g^{-1}). Moreover, when the current density returns to 50 mA g^{-1}, the capacity recovers well to a high value of 91.6 mAh g^{-1}, which is much higher than those cycled in 1 M NaAc-Di (41.6 mAh g^{-1}), indicating its excellent reversibility. The long-term cycling stability of NMO plates cycled in different electrolytes are further examined. As shown in Figure 3g, the NMO electrode cycled in 1 M NaAc-Et/Di displays a high initial capacity of 76 mAh g^{-1} at 100 mA g^{-1}. After 100 cycles, the NMO electrode retains a high reversible capacity of 75 mAh g^{-1} with a capacity retention of 99 %, which is > 2 times

higher than that in 1 M NaAc-Di (48%). Unexpectedly, the cycling stability is also superior to that of the "water-in-salt" 9.26 m $NaCF_3SO_3$ and 17 m $NaClO_4$ electrolytes (capacity retention of 27.4% and 25.6%, respectively). Moreover, even after 1000 cycles, the NMO cycled in 1 M NaAc-Et/Di exhibit excellent cycling stability with a capacity decay rate per cycle of 0.024% at 100 mA g^{-1}, which is much lower than that of NMO electrode cycled in 1 M NaAc-Di (0.087%). This can be ascribed to the reduced water protons activity induced by the intrinsic hydrogen-bonding between the ethanol oxygen and water protons in Et/Di system. Moreover, the 1 M NaAc in Et/Di electrolyte provides superior wetting characteristics. As displayed in Figure S9, due to the presence of ethanol, the contact angle of 1 M NaAc in Et/Di electrolyte on stainless steel is only 22.4°, much lower than that of 1 M NaAc in Di electrolyte (83.3°) and also lower than that of "water-in-salt" 9.26 m $NaCF_3SO_3$ (79.4°) and 17 m $NaClO_4$ electrolytes (101.1°), demonstrating the hydrophilic property of 1 M NaAc in Et/Di electrolyte, which can effectively facilitate the electrolyte penetration into the electrode and thus improve the electrochemical performance. Therefore, good wettability, excellent rate capability, and long-term cycling performance make the Et/Di system a promising electrolyte candidate for applicable ARSIBs.

To shed light on the charge storage mechanism of NMOs cycled in the Et/Di and Di systems, XRD, SEM, and TEM-EDS mapping measurements were conducted after different cycles. In comparison to the pristine morphology, NMO plates exhibit partial fragmentation with a rough surface after five cycles when cycled in the Di system, as shown in Figure 4a. As discussed above in the XANES section, the disproportionation of Mn^{3+} leads to the formation of soluble Mn^{2+} species. Thus, NMO suffers a significant capacity loss in the initial cycles due to the dissolution of electrochemical active NMO in Di system. By contrast, the NMO plate structure remains a smooth surface after cycled in the Et/Di system (Figure 4b), indicating that the introduction of ethanol in the electrolyte plays a critical role in stabilizing the NMO electrode

structure. *Ex-situ* XRD characterizations were further performed to explore the storage mechanism of NMO cycled in both Et/Di and Di systems (Figures 4e and S10). As shown in Figure S10, the NMO still maintains the $Na_{0.44}MnO_2$ (PDF 04-018-3147) phase with *Pbam* space group when cycled in Di system after 100 cycles, Notably, compared with the pristine electrode, a broad new diffraction peak located at around 26° appears after 200 cycles, which can be indexed to MnOOH (PDF 04-010-4788), demonstrating an irreversible de/insertion of sodium-ions in NMO upon cycling. When cycled after 500 cycles, the product remains a mixed phase. Eventually, the NMO totally transformed to MnOOH after 1000 cycles, as demonstrated by the XRD pattern in Figures S10 and 4e. In contrast, all the diffraction peaks of NMO cycled in Et/Di system after 1000 cycles are still consistent with that of the pristine electrode $Na_{0.44}MnO_2$ (PDF 04-018-3147), indicating the excellent structure stability of NMO in Et/Di system. Based on the results, it is proposed that the NMO cycled in the Et/Di system undergoes reversible desodiation/sodiation processes as described below:

$$Na_{0.44}MnO_2 + xNa^+ + xe^- \leftrightarrow Na_{0.44+x}MnO_2 \qquad (1)$$

In the Di system, sodium-ions and water protons are co-intercalated into the NMO structure during the discharge process. However, the existence of protons could induce electrostatic repulsion with sodium-ions in the NMO lattice,[42] which hinders sodium-ions insertion. The details of the reactions can be formulated as follows:

$$Na_{0.44}MnO_2 + xNa^+ + xe^- \leftrightarrow Na_{0.44+x}MnO_2 \qquad (2)$$

$$Na_{0.44}MnO_2 + yH^+ + ye^- \rightarrow Na_{0.44}H_yMnO_2 \qquad (3)$$

Ex-situ TEM, selected area electron diffraction (SAED), and TEM-EDS analysis provide further proof for the storage mechanism of NMO cycled in both Et/Di and Di system after 1000 cycles. SEM and enlarged TEM images (Figures S11 and 4c) reveal that the product of NMO cycled in Di system after 1000 cycles is composed of distributed nanorods with widths of 100 nm and lengths of ~1 μm. The diffraction spots in the SAED pattern (Figure S12a) can be

indexed to the (-111) and (002) planes of MnOOH. High-resolution TEM (HRTEM) image taken on the nanorod shows well-resolved lattice fringes with an interplanar distance of 0.34 nm (inset in Figure 4c), corresponding to the (-111) crystal plane of manganese oxohydroxide (MnOOH), which is consistent with the XRD result. The corresponding TEM-EDS mapping (Figure S13) reveals the existence of Mn and O elements in the newly formed nanorods, whereas traces of Na have almost disappeared, further confirming the formation of manganese oxohydroxide after long-term cycling. As discussed above, the fragmentation is caused by the dissolution of Mn^{2+} species formed during the disproportionation reaction of Mn^{3+} when water protons and sodium-ions co-insert into the structure. As a result, the irreversible protons insertion causes a steady accumulation of manganese oxohydroxide, leading to poor electrochemical performance. By contrast, as shown in Figure 4d, the TEM image of NMO cycled in the Et/Di system reveals that the plate morphology is still well-maintained. SAED pattern in Figure S12b reveals that the plates are single-crystalline structure with the orientation along the [001] direction. HR-TEM image (inset of Figure 4d) displays a lattice spacing of 0.45 nm, corresponding to the (200) plane of $Na_{0.44}MnO_2$. The TEM-EDS elemental mapping images of NMO cycled in the Et/Di system further demonstrate the uniform distribution of Mn, O, and especially Na elements in the cycled NMO (Figure 4f).

In addition, the Et/Di hybrid electrolyte can be applied in a wide temperature range. As demonstrated, the $Na_{0.44}MnO_2$/Zn full cells in 1 M NaAc-Et/Di electrolyte were assembled and cycled between 0.65 and 1.75 V at 25 °C and 0 °C, as shown in Figure 5. It delivers a high discharge capacity of 93 mAh g^{-1} on the 2nd cycle at 25 °C, corresponding to a high energy density of 102 Wh kg^{-1} (Figure 5a). It also exhibits excellent cycling stability with a high capacity retention of 99.8% after 50 cycles at 100 mA g^{-1} (Figure 5b). Moreover, the full cell displays good rate capability (Figure 5c). As the current density increases to 500 mA g^{-1}, the discharge capacity of the NMO remains at 42.7 mAh g^{-1}. When the current density returns to

100 mA g^{-1}, the discharge capacity recovers to 90.2 mAh g^{-1}, demonstrating its good rate capability. When further tested at 0 °C, the full cell retains a discharge capacity of 44.5 mAh g^{-1} after 50 cycles with a capacity retention of 94% at 50 mA g^{-1} (Figure 5d). Compared with the recently reported sodium-ion batteries (Figure 5e), the full cell exhibits impressive energy density (102 Wh kg^{-1}).[5, 52-58]

Herein, we discuss the reason accounting for the much higher cycling stability and rate capability of NMO cycled in the Et/Di system. The ions storage and structural evolution of NMO cycled in Et/Di and Di systems are displayed schematically in Scheme 1. Owing to the hydrogen-bonding interactions in Et/Di system, most of the proton atoms in water molecules are strongly bonded with the hydroxyl oxygens in ethanol (Scheme 1a). In contrast, abundant water molecules exist in Di system, providing a proton-rich environment (Scheme 1b). During the sodiation process, not only the Na ions, protons can co-insert into the tunnels of the NMO electrode. Then, NMO suffers the dissolution of Mn^{2+} induced by disproportionation reaction and irreversible phase transformation to MnOOH (Scheme 1b). This explains the rapid capacity fading and poor cycling stability of NMO in Di water system. In contrast, in Et/Di system, water protons activity has been effectively suppressed by the existing hydrogen bonds with ethanol oxygens (Scheme 1a). Therefore, Na ions can reversibly de/insert into the NMO structure, resulting in much higher cycling stability and rate capability.

Conclusions

In summary, we reported a novel type of ethanol-water system for hybrid electrolyte formulations. Coupled with different low concentrated sodium-based salts, such green and low-cost electrolytes enable Na-ion chemistry with superior electrochemical performances, especially in terms of cycling stability. Benefiting from the formation of hydrogen-bonding interactions, the introduction of ethanol improves surface wettability, suppresses water protons

activities, and reduces transition metal dissolution from the cathode, facilitating highly reversible sodium-ion de/intercalation processes in a wide temperature range. This hybrid electrolyte enables $Na_{0.44}MnO_2$ electrodes to achieve a high capacity of 81 mAh g^{-1} and excellent cycling stability with a capacity decay rate per cycle of 0.024% at 100 mA g^{-1} for 1000 cycles, four times better than that in the water-based electrolyte. Additionally, compared with the irreversible phase transformation from $Na_{0.44}MnO_2$ to MnOOH when cycled in the water-based electrolyte, the $Na_{0.44}MnO_2$ still maintains its original phase when cycled in the ethanol-water system, further confirming its structural stability. Overall, we have demonstrated the strategy of hydrogen bonded hybridization creates novel electrolyte systems that enable vastly improved electrochemical performances and may open doors for greener electrolytes in aqueous rechargeable sodium-ion batteries and others.

Acknowledgments

The authors wish to acknowledge financial support from by National Research Foundation of Singapore (NRF) Investigatorship award number NRFI2017-08/NRF2016NRF-NRFI001-22. This research used the Beamline 28-ID-2 X-ray powder diffraction (XPD) of the National Synchrotron Light Source II, a U.S. Department of Energy (DOE) Office of Science User Facility operated for the DOE Office of Science by Brookhaven National Laboratory under Contract No. DE-SC0012704. The authors thank Synchrotron Light Research Institute (Public Organization), Muang, Nakhon Ratchasima, 30000, Thailand, for XANES measurements in Beamline 5.2. Rodney Chua and Yi Cai contributed equally to this work.

Supporting Information

Experimental section; Cost comparison of various electrolytes based on different salts; Raman scattering spectra of pure water and ethanol-water co-solvents and the corresponding mode of vibrations; FTIR-ATR absorption spectra and NMR chemical shifts of water-ethanol co-solvents; Calculated integrated proton ratios in the pure ethanol and ethanol-water co-solvents; Occupancy of each atomic site refined by the Rietveld method of the as-synthesized NMO; Electrochemical performances of the NMO; Contact angles of different electrolytes; *Ex-situ* XRD, SEM images, SAED patterns, TEM-EDS elemental mappings of cycled NMO products

References

(1) Demir-Cakan, R.; Palacin, M. R.; Croguennec, L. Rechargeable Aqueous Electrolyte Batteries: From Univalent to Multivalent Cation Chemistry. *J. Mater. Chem. A* **2019**, *7* (36), 20519-20539.

(2) Huang, J.; Guo, Z.; Ma, Y.; Bin, D.; Wang, Y.; Xia, Y. Recent Progress of Rechargeable Batteries Using Mild Aqueous Electrolytes. *Small Methods* **2019**, *3* (1), 1800272.

(3) Yamada, Y.; Wang, J.; Ko, S.; Watanabe, E.; Yamada, A. Advances and Issues in Developing Salt-Concentrated Battery Electrolytes. *Nat. Energy* **2019**, *4* (4), 269-280.

(4) Kim, H.; Hong, J.; Park, K.-Y.; Kim, H.; Kim, S.-W.; Kang, K. Aqueous Rechargeable Li and Na Ion Batteries. *Chem. Rev.* **2014,** *114* (23), 11788-11827.

(5) Suo, L.; Borodin, O.; Wang, Y.; Rong, X.; Sun, W.; Fan, X.; Xu, S.; Schroeder, M. A.; Cresce, A. V.; Wang, F. "Water-in-Salt" Electrolyte Makes Aqueous Sodium-Ion Battery Safe, Green, and Long-Lasting. *Adv. Energy Mater.* **2017**, *7* (21), 1701189.

(6) Kühnel, R.-S.; Reber, D.; Battaglia, C. A High-Voltage Aqueous Electrolyte for Sodium-Ion Batteries. *ACS Energy Letters* **2017**, *2* (9), 2005-2006.

(7) Nakamoto, K.; Sakamoto, R.; Sawada, Y.; Ito, M.; Okada, S. Over 2 V Aqueous Sodium-Ion Battery with Prussian Blue-Type Electrodes. *Small Methods* **2019**, *3* (4), 1800220.

(8) Zheng, Q.; Miura, S.; Miyazaki, K.; Ko, S.; Watanabe, E.; Okoshi, M.; Chou, C. P.; Nishimura, Y.; Nakai, H.; Kamiya, T. Sodium - and Potassium - Hydrate Melts Containing Asymmetric Imide Anions for High-Voltage Aqueous Batteries. *Angew. Chem. Int. Ed.* **2019**, 14202-14207.

(9) Fecko, C. J.; Loparo, J. J.; Roberts, S. T.; Tokmakoff, A. Local Hydrogen Bonding Dynamics and Collective Reorganization in Water: Ultrafast Infrared Spectroscopy of HOD/D_2O. *J. Chem. Phys.* **2005**, *122* (5), 054506.

(10) Mohsen-Nia, M.; Amiri, H.; Jazi, B. Dielectric Constants of Water, Methanol, Ethanol, Butanol and Acetone: Measurement and Computational Study. *J. Solution Chem.* **2010**, *39* (5), 701-708.

(11) Lide, D. R. *Crc Handbook of Chemistry and Physics*, CRC press: Washington, DC, **2004**; Vol. 85, pp 15-16.

(12) Mizuno, K.; Miyashita, Y.; Shindo, Y.; Ogawa, H. NMR and FT-IR Studies of Hydrogen Bonds in Ethanol-Water Mixtures. *J. Phys. Chem.* **1995**, *99* (10), 3225-3228.

(13) Burikov, S.; Dolenko, T.; Patsaeva, S.; Starokurov, Y.; Yuzhakov, V. Raman and IR Spectroscopy Research on Hydrogen Bonding in Water–Ethanol Systems. *Mol. Phys.* **2010**, *108* (18), 2427-2436.

(14) Nose, A.; Hojo, M.; Ueda, T. Effects of Salts, Acids, and Phenols on the Hydrogen-Bonding Structure of Water− Ethanol Mixtures. *J. Phys. Chem. B* **2004,** *108* (2), 798-804.

(15) Meng, L. Ethanol in Automotive Applications. *Ethanol*; Elsevier: Tempe, Arizona, **2019**; pp 289-303.

(16) Wu, N.; Li, X.; Liu, S.; Zhang, M.; Ouyang, S. Effect of Hydrogen Bonding on the Surface Tension Properties of Binary Mixture (Acetone-Water) by Raman Spectroscopy. *Appl. Sci.* **2019**, *9* (6), 1235.

(17) Ghoufi, A.; Artzner, F.; Malfreyt, P. Physical Properties and Hydrogen-Bonding Network of Water–Ethanol Mixtures from Molecular Dynamics Simulations. *J. Phys. Chem. B* **2016**, *120* (4), 793-802.

(18) Dou, Q.; Lu, Y.; Su, L.; Zhang, X.; Lei, S.; Bu, X.; Liu, L.; Xiao, D.; Chen, J.; Shi, S. A Sodium Perchlorate-Based Hybrid Electrolyte with High Salt-to-Water Molar Ratio for Safe 2.5 V Carbon-Based Supercapacitor. *Energy Storage Mater.* **2019**, *23, 603-609*.

(19) Li, F.; Men, Z.; Li, S.; Wang, S.; Li, Z.; Sun, C. Study of Hydrogen Bonding in Ethanol-Water Binary Solutions by Raman Spectroscopy. *Spectrochim. Acta A* **2018**, *189*, 621-624.

(20) Scherer, J. R.; Go, M. K.; Kint, S. Raman Spectra and Structure of Water from -10 to 90. Deg. *J. Phys. Chem.* **1974**, *78* (13), 1304-1313.

(21) Giguère, P. A. Bifurcated Hydrogen Bonds in Water. *J. Raman Spectrosc.* **1984**, *15* (5), 354-359.

(22) Du, Q.; Freysz, E.; Shen, Y. R. Vibrational Spectra of Water Molecules at Quartz/Water Interfaces. *Phys. Rev. Lett.* **1994**, *72* (2), 238.

(23) Nose, A.; Hojo, M. Hydrogen Bonding of Water–Ethanol in Alcoholic Beverages. *J. Biosci. and Bioeng.* **2006**, *102* (4), 269-280.

(24) Falk, M. The Frequency of the H-O-H Bending Fundamental in Solids and Liquids. *Spectrochim. Acta A* **1984**, *40* (1), 43-48.

(25) Demir, A., Nmr-the Basic Principles and Its Use in Studies of Water/Ethanol/Mixture. Bachelor Degree Thesis, Umeå University, April **2012**.

(26) Wang, Y.; Liu, J.; Lee, B.; Qiao, R.; Yang, Z.; Xu, S.; Yu, X.; Gu, L.; Hu, Y.-S.; Yang, W. Ti-Substituted Tunnel-Type $Na_{0.44}MnO_2$ Oxide as a Negative Electrode for Aqueous Sodium-Ion Batteries. *Nat. Commun.* **2015**, *6* (1), 1-10.

(27) Jiang, C.; Tang, Z.; Wang, S.; Zhang, Z. A Truncated Octahedral Spinel $LiMn_2O_4$ as High-Performance Cathode Material for Ultrafast and Long-Life Lithium-Ion Batteries. *J. Power Sources* **2017**, *357*, 144-148.

(28) Jiang, L.; Wu, Z.; Wang, Y.; Tian, W.; Yi, Z.; Cai, C.; Jiang, Y.; Hu, L. Ultrafast Zinc-Ion Diffusion Ability Observed in 6.0-Nanometer Spinel Nanodots. *ACS nano* **2019**, *13* (9), 10376-10385.

(29) Kim, D. J.; Ponraj, R.; Kannan, A. G.; Lee, H.-W.; Fathi, R.; Ruffo, R.; Mari, C. M.; Kim, D. K. Diffusion Behavior of Sodium Ions in $Na_{0.44}MnO_2$ in Aqueous and Non-Aqueous Electrolytes. *J. Power Sources* **2013**, *244*, 758-763.

(30) Doeff, M. M.; Anapolsky, A.; Edman, L.; Richardson, T. J.; De Jonghe, L. A High-Rate Manganese Oxide for Rechargeable Lithium Battery Applications. *J. Electrochem. Soc.* **2001**, *148* (3), A230-A236.

(31) Cao, Y.; Xiao, L.; Wang, W.; Choi, D.; Nie, Z.; Yu, J.; Saraf, L. V.; Yang, Z.; Liu, J. Reversible Sodium Ion Insertion in Single Crystalline Manganese Oxide Nanowires with Long Cycle Life. *Adv. Mater.* **2011**, *23* (28), 3155-3160.

(32) Ma, G.; Zhao, Y.; Huang, K.; Ju, Z.; Liu, C.; Hou, Y.; Xing, Z. Effects of the Starting Materials of $Na_{0.44}MnO_2$ Cathode Materials on Their Electrochemical Properties for Na-Ion Batteries. *Electrochim. Acta* **2016**, *222*, 36-43.

(33) Sauvage, F.; Laffont, L.; Tarascon, J.-M.; Baudrin, E. Study of the Insertion/Deinsertion Mechanism of Sodium into $Na_{0.44}MnO_2$. *lnorg. Chem.* **2007**, *46* (8), 3289-3294.

(34) Akimoto, J.; Hayakawa, H.; Kijima, N.; Awaka, J.; Funabiki, F. Single-Crystal Synthesis and Structure Refinement of $Na_{0.44}MnO_2$, *Solid State Phenom*, **2011**, *170*, 198-202.

(35) Chua, R.; Cai, Y.; Kou, Z. K.; Satish, R.; Ren, H.; Chan, J. J.; Zhang, L.; Morris, S. A.; Bai, J.; Srinivasan, M. 1.3 V Superwide Potential Window Sponsored by Na-Mn-O Plates as Cathodes Towards Aqueous Rechargeable Sodium-Ion Batteries. *Chem. Eng. J.* **2019**, *370*, 742-748.

(36) Jiang, C.; Wang, S.; Li, Y.; Zhang, Z.; Tang, Z. A Layered-Spinel Lithium Manganite Hydrate for High-Capacity and Ultrafast Lithium Storage. *J. Power Sources* **2019**, *413*, 441-448.

(37) Whitacre, J.; Tevar, A.; Sharma, S. $Na_4Mn_9O_{18}$ as a Positive Electrode Material for an Aqueous Electrolyte Sodium-Ion Energy Storage Device. *Electrochem. Commun.* **2010**, *12* (3), 463-466.

(38) Ma, G.; Zhao, Y.; Huang, K.; Ju, Z.; Liu, C.; Hou, Y.; Xing, Z. Effects of the Starting Materials of $Na_{0.44}MnO_2$ Cathode Materials on Their Electrochemical Properties for Na-Ion Batteries. *Electrochim. Acta* **2016**, *222*, 36-43.

(39) Wang, Y.; Wu, Z.; Jiang, L.; Tian, W.; Zhang, C.; Cai, C.; Hu, L. A Long-Lifespan, Flexible Zinc-Ion Secondary Battery Using a Paper-Like Cathode from Single-Atomic Layer MnO_2 Nanosheets. *Nanoscale Advances* **2019**, *1* (11), 4365-4372.

(40) Zhao, Y.; Hu, L.; Zhao, S.; Wu, L. Preparation of $MnCo_2O_4$@$Ni(OH)_2$ Core–Shell Flowers for Asymmetric Supercapacitor Materials with Ultrahigh Specific Capacitance. *Adv. Funct. Mater.* **2016**, *26* (23), 4085-4093.

(41) Chu, Q.; Wang, X.; Li, Q.; Liu, X. The Tunnel Manganese Oxide $Na_{4.32}Mn_9O_{18}$: A New Na^+ Site Discovered by Single-Crystal X-Ray Diffraction. *Acta Crystallogr. Sect. C: Cryst. Struct. Commun.* **2011**, *67* (2), i10-i12.

(42) Kim, H.; Kim, D. J.; Seo, D.-H.; Yeom, M. S.; Kang, K.; Kim, D. K.; Jung, Y. Ab Initio Study of the Sodium Intercalation and Intermediate Phases in $Na_{0.44}MnO_2$ for Sodium-Ion Battery. *Chem. Mater.* **2012**, *24* (6), 1205-1211.

(43) Momma, K.; Izumi, F. Vesta 3 for Three-Dimensional Visualization of Crystal, Volumetric and Morphology Data. *J. Appl. Crystallogr.* **2011**, *44* (6), 1272-1276

(44) Wongittharom, N.; Wang, C.-H.; Wang, Y.-C.; Yang, C.-H.; Chang, J.-K. Ionic Liquid Electrolytes with Various Sodium Solutes for Rechargeable Na/$NaFePO_4$ Batteries Operated at Elevated Temperatures. *ACS Appl. Mater.* **2014**, *6* (20), 17564-17570.

(45) Wang, C.-H.; Yeh, Y.-W.; Wongittharom, N.; Wang, Y.-C.; Tseng, C.-J.; Lee, S.-W.; Chang, W.-S.; Chang, J.-K. Rechargeable Na/$Na_{0.44}MnO_2$ Cells with Ionic Liquid Electrolytes Containing Various Sodium Solutes. *J. Power Sources* **2015**, *274*, 1016-1023.

(46) Hasa, I.; Passerini, S.; Hassoun, J. Characteristics of an Ionic Liquid Electrolyte for Sodium-Ion Batteries. *J. Power Sources* **2016**, *303*, 203-207.

(47) Ding, C.; Nohira, T.; Kuroda, K.; Hagiwara, R.; Fukunaga, A.; Sakai, S.; Nitta, K.; Inazawa, S. NaFSA–C1C3pyrFSA Ionic Liquids for Sodium Secondary Battery Operating over a Wide Temperature Range. *J. Power Sources* **2013**, *238*, 296-300.

(48) Bhide, A.; Hofmann, J.; Dürr, A. K.; Janek, J.; Adelhelm, P. Electrochemical Stability of Non-Aqueous Electrolytes for Sodium-Ion Batteries and Their Compatibility with $Na_{0.7}CoO_2$. *Phys. Chem. Chem. Phys.* **2014**, *16* (5), 1987-1998.

(49) Dall'Asta, V.; Buchholz, D.; Chagas, L. G.; Dou, X.; Ferrara, C.; Quartarone, E.; Tealdi, C.; Passerini, S. Aqueous Processing of $Na_{0.44}MnO_2$ Cathode Material for the Development of Greener Na-Ion Batteries. *ACS Appl. Mater.* **2017**, *9* (40), 34891-34899.

(50) Chalmin, E.; Farges, F.; Brown, G. E. A Pre-Edge Analysis of Mn K-Edge Xanes Spectra to Help Determine the Speciation of Manganese in Minerals and Glasses. *Contrib. Mineral. Petrol.* **2009**, *157* (1), 111-126.

(51) Huang, J.; Guo, Z.; Dong, X.; Bin, D.; Wang, Y.; Xia, Y. Low-Cost and High Safe Manganese-Based Aqueous Battery for Grid Energy Storage and Conversion. *Sci. Bull.* **2019**, *64* (23), 1780-1787.

(52) Kumar, P. R.; Jung, Y. H.; Wang, J. E.; Kim, D. K. $Na_3V_2O_2(PO_4)_2F$-MWCNT Nanocomposites as a Stable and High Rate Cathode for Aqueous and Non-Aqueous Sodium-Ion Batteries. *J. Power Sources* **2016**, *324*, 421-427.

(53) Wu, X.; Cao, Y.; Ai, X.; Qian, J.; Yang, H. A Low-Cost and Environmentally Benign Aqueous Rechargeable Sodium-Ion Battery Based on $NaTi_2(PO_4)_3$–$Na_2NiFe(CN)_6$ Intercalation Chemistry. *Electrochem. Commun.* **2013**, *31*, 145-148.

(54) Wang, L.-P.; Wang, P.-F.; Wang, T.-S.; Yin, Y.-X.; Guo, Y.-G.; Wang, C.-R. Prussian Blue Nanocubes as Cathode Materials for Aqueous Na-Zn Hybrid Batteries. *J. Power Sources* **2017**, *355*, 18-22.

(55) Li, Z.; Ravnsbæk, D. B.; Xiang, K.; Chiang, Y.-M. $Na_3Ti_2(PO_4)_3$ as a Sodium-Bearing Anode for Rechargeable Aqueous Sodium-Ion Batteries. *Electrochem. Commun.* **2014**, *44*, 12-15.

(56) Nakamoto, K.; Kano, Y.; Kitajou, A.; Okada, S. Electrolyte Dependence of the Performance of a $Na_2FeP_2O_7$//$NaTi_2(PO_4)_3$ Rechargeable Aqueous Sodium-Ion Battery. *J. Power Sources* **2016**, *327*, 327-332.

(57) Liu, Y.; Zhang, B.; Xiao, S.; Liu, L.; Wen, Z.; Wu, Y. A Nanocomposite of MoO_3 Coated with PPy as an Anode Material for Aqueous Sodium Rechargeable Batteries with Excellent Electrochemical Performance. *Electrochim. Acta* **2014**, *116*, 512-517.

(58) Pasta, M.; Wessells, C. D.; Liu, N.; Nelson, J.; McDowell, M. T.; Huggins, R. A.; Toney, M. F.; Cui, Y. Full Open-Framework Batteries for Stationary Energy Storage. *Nat. Commun.* **2014**, *5* (1), 1-9.

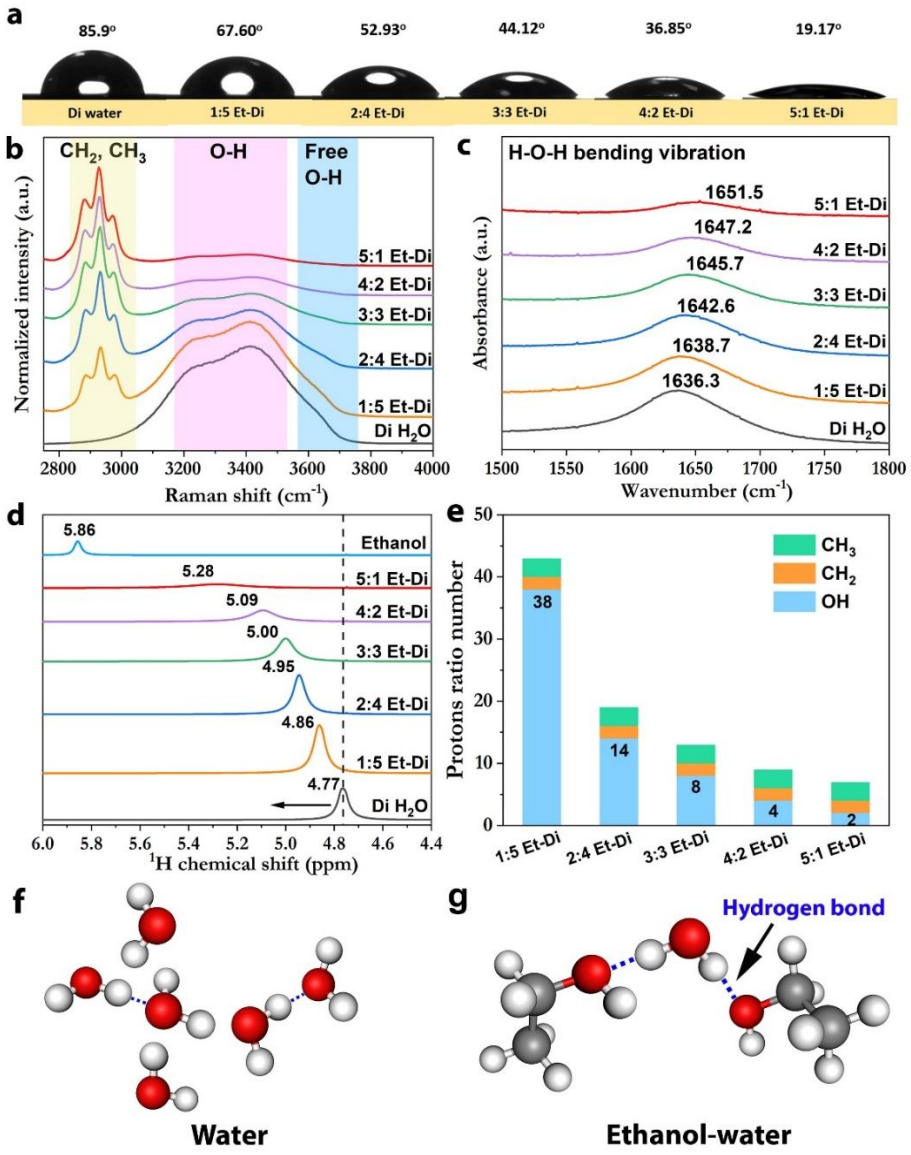

Figure 1. The bulk properties of the ethanol-water system with different concentrations. (a) Contact angles comparison, (b) confocal Raman and (c) Fourier transform infrared red-attenuated total reflectance (FTIR-ATR) spectra of water and ethanol-water solvents, (d) chemical shifts for ^{1}H nuclei in Di water, ethanol and ethanol-water solvents, (e) integrated proton ratio number of protons in the different hydrogen atoms environment (CH_2, CH_3, OH) of ethanol-water solvents and schematics of (f) water and (g) ethanol-water intermolecular interactions.

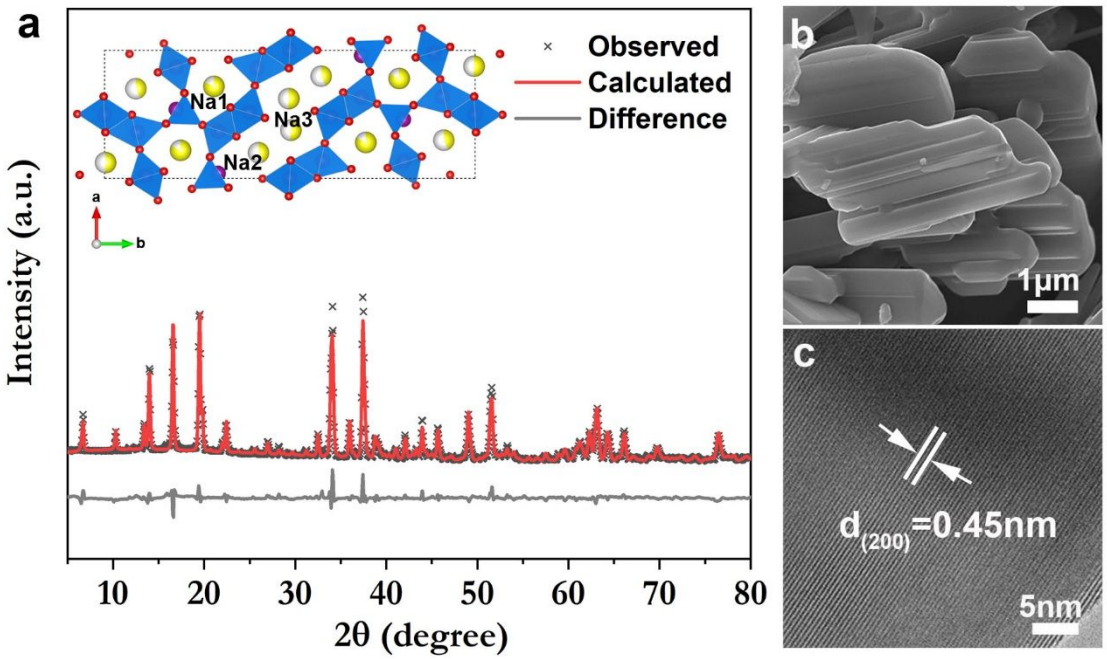

Figure 2. Structural characterizations of $Na_{0.44}MnO_2$. (a) High-resolution synchrotron-based XRD powder diffraction of $Na_{0.44}MnO_2$ plates with its corresponding unit cell (inset of a), (b) SEM image, and (c) high-resolution TEM (HRTEM) image of NMO plates.

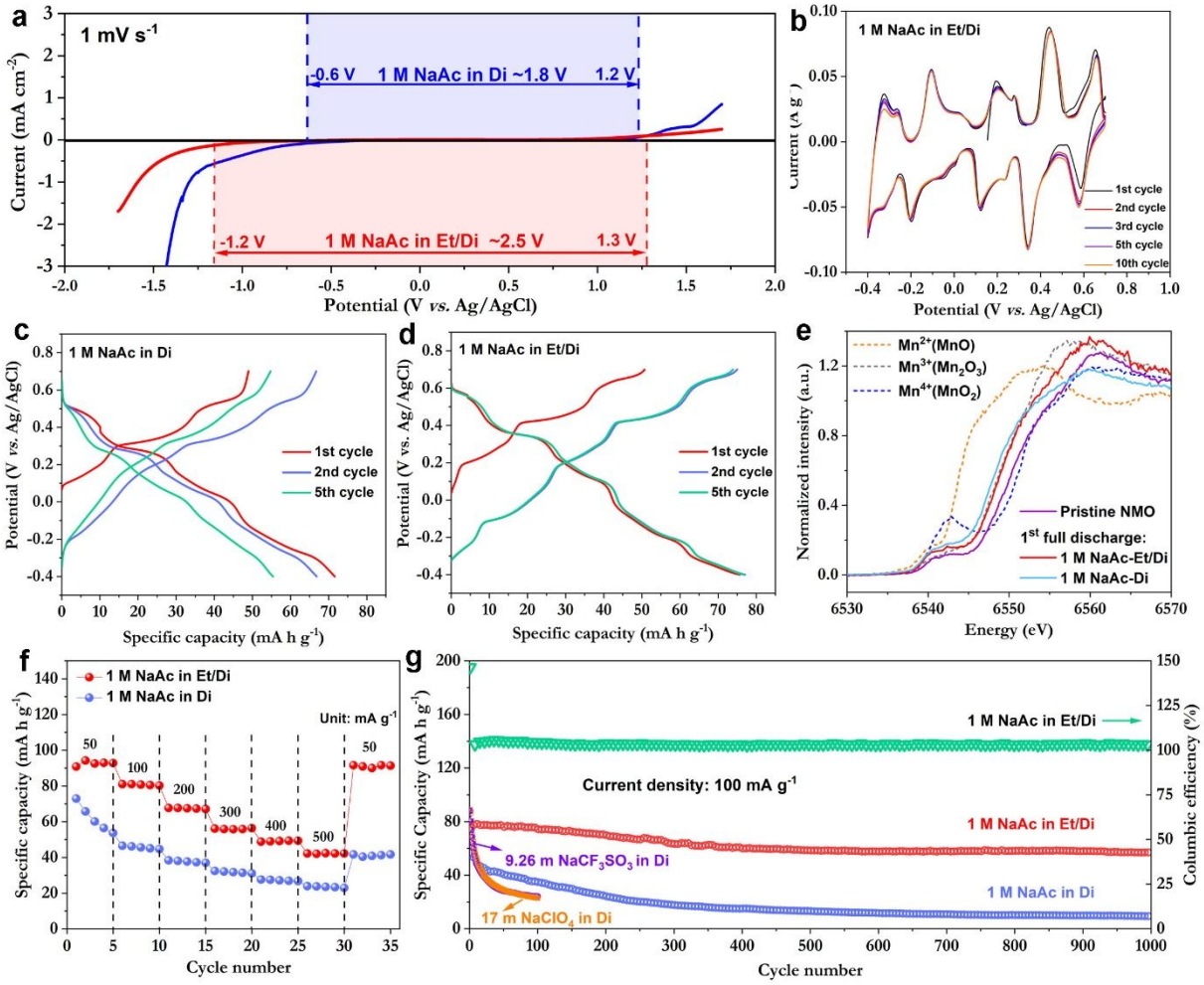

Figure 3. Electrochemical performances of the $Na_{0.44}MnO_2$ plates in different electrolytes. (a) Electrochemical stability of 1 M NaAc in Et/Di and 1 M NaAc in Di electrolytes. Cyclic voltammetry profiles of NMO cycled in (b) 1 M NaAc-Et/Di, typical galvanostatic charge-discharge profiles (1st, 2nd and 5th cycles) of NMO cycled in (c) 1 M NaAc-Di and (d) 1 M NaAc-Et/Di, (e) XANES curves of NMOs in pristine and full discharge states, (f) rate capability comparison and (g) long term cycling performances of NMOs at 100 mA g^{-1}.

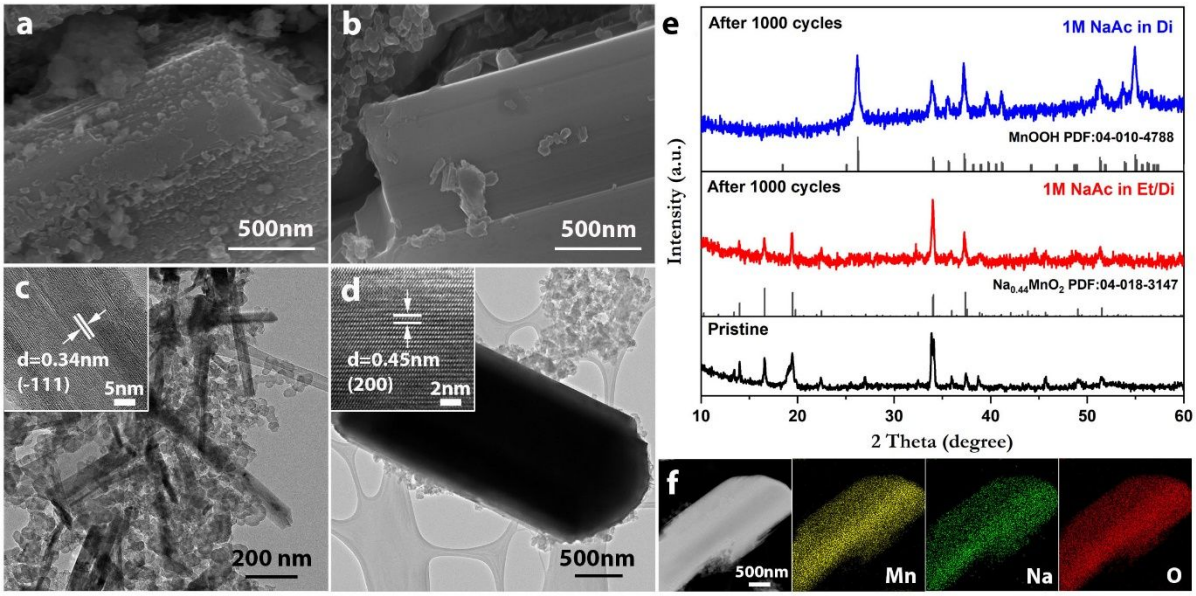

Figure 4. Postmortem characterizations of cycled $Na_{0.44}MnO_2$ electrodes. (a, b) SEM images of NMO electrodes cycled in 1 M NaAc in Di, and 1 M NaAc in Et/Di after 5cycles, respectively, (c, d) TEM and HRTEM (inset) images of NMO cycled in 1 M NaAc in Di, and 1 M NaAc in Et/Di after 1000 cycles, respectively, (e) XRD patterns of pristine and cycled electrodes, and (f) TEM-EDS elemental mappings of NMO cycled in 1 M NaAc in Et/Di after 1000 cycles.

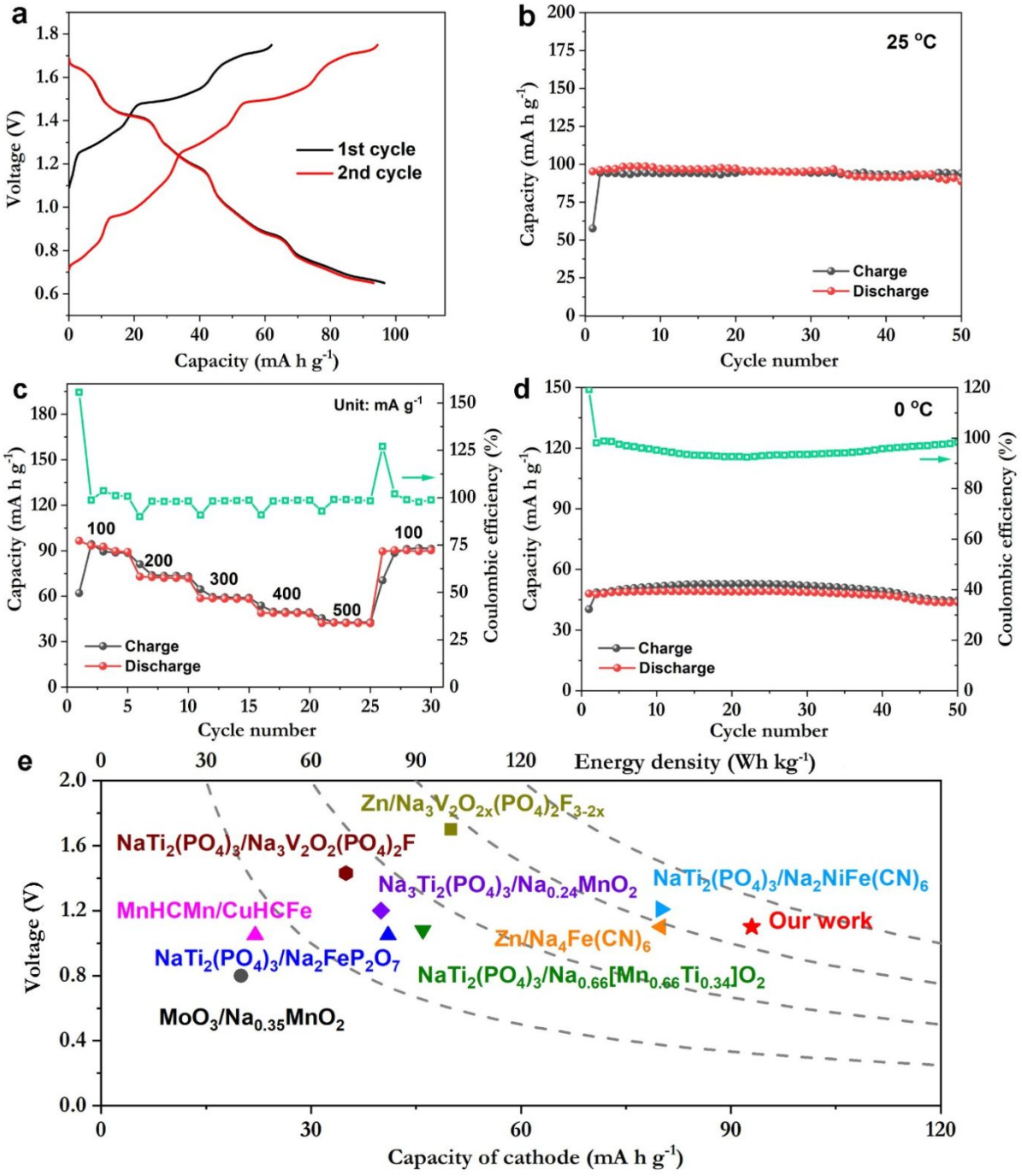

Figure 5. Electrochemical performances of $Na_{0.44}MnO_2$/Zn full cells in 1 M NaAc in Et/Di electrolyte. a) Charge-discharge profiles at 100 mA g^{-1}, b) cycling stability of full cell at 100 mA g^{-1} at 25 °C, c) rate capability, and d) cycling stability of full cell at 0 °C. The cells were cycled within the voltage range of 0.65 to 1.75 V. e) Comparison of capacity and energy density reported for aqueous sodium-ion batteries. (Energy densities are calculated based on the cathode from the reported papers)[5, 52-58]

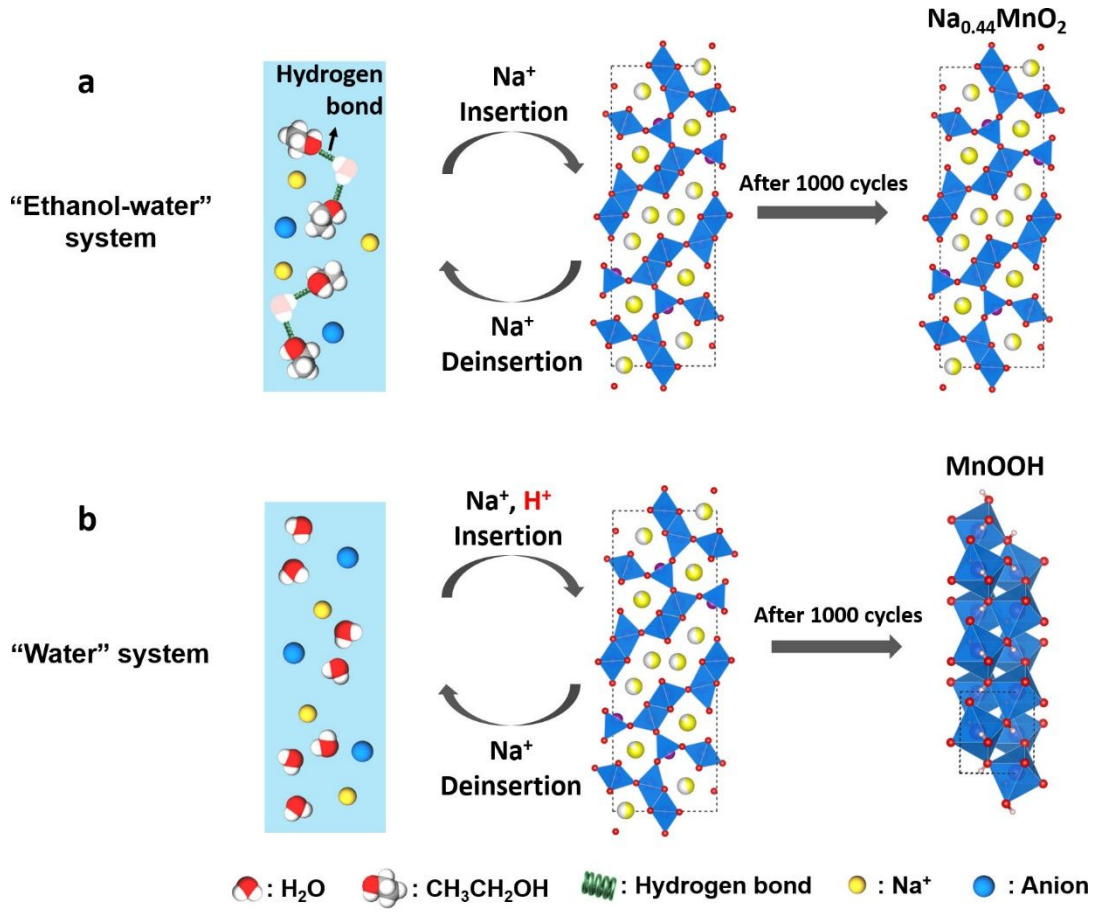

Scheme 1. Schematics illustration of ions storage in (a) ethanol-water and (b) water systems. The lighter coloring of H_2O molecules in the ethanol-water system (scheme 1a) represents the suppressed water protons activity as compared to that in the water system (scheme 1b).

For Table of Contents Only